CFD MODEL OF BUBBLE DRIVEN FLOW IN ALUMINIUM REDUCTION CELLS AND VALIDATION USING PIV MEASUREMENT

Y.Q. FENG, W. YANG, M. COOKSEY and M.P. SCHWARZ

CSIRO Minerals, Clayton, Victoria 3169, AUSTRALIA

ABSTRACT

This paper presents a CFD modelling study of the bubble driven hydrodynamics in aluminium reduction cells. A time-averaged (steady state) bubble driven flow model has been developed using a full scale air-water model of part of an aluminium reduction cell as a test-bed. Simulated results have been compared with experimental data taken under similar conditions using Particle Image Velocimetry (PIV). Good agreement has been obtained between the CFD model and the PIV measurements, which demonstrates the validity of extending the current CFD model to study the effect of various design parameters (e.g. inter-anode gap, insertion of a slot) on bath flow in an industrial cell. Overall flow beneath the anode has been investigated in terms of streamlines calculated from both CFD simulation and PIV measurement. It was found that the water flow is very complex and is significantly affected by end channel width.

NOMENCLATURE

$C_{\mu p}$ bubble induced turbulent eddy viscosity coefficient [-]

C_{TD} turbulent dispersion force coefficient [-]

C_{CD} drag force coefficient [-]

d bubble diameter [m]

k turbulent kinetic energy [m^2s^{-2}]

M_α interfacial momentum transfer between phases [$kg\ m^{-1}s^{-2}$]

M^{TD} Turbulent dispersion force [Nm^{-3}]

P pressure [Pa]

$S_{M\alpha}$ momentum sources due to external body forces [$kg\ m^{-1}\ s^{-2})$]

U velocity [$m\ s^{-1}$]

γ volume fraction [-]

ε turbulent energy dissipation rate [m^2s^{-3}]

ρ density [$kg\ m^{-3}$]

μ dynamic viscosity [Pa·s]

μ_t turbulent eddy viscosity [Pa·s]

μ_{tp} bubble induced turbulent eddy viscosity [Pa·s]

SUBSCRIPT

c continuous liquid phase

d dispersed gas phase

t turbulence

α phase, either gas (g) or water (w)

INTRODUCTION

The aluminium reduction cell, or Hall-Heroult cell, is the main unit for primary aluminium production, and utilises a very complex process involving electro-chemical reactions, hydrodynamics driven by anodic gases and electromagnetic force, and complex heat transfer. The main aspects relevant to this paper are as follows.

Alumina is fed to, and dissolved in, a molten bath of cryolite at approximately 970ºC in which several anodes are submerged. Electric current is fed between the anodes and an underlying cathode to cause electrochemical reduction of the alumina to aluminium which settles onto a pool lying over the cathode. CO_2 gas bubbles are generated by the reaction at the anode, and in moving up through the molten cryolite (the bath) under the influence of buoyancy, recirculation flows are set up. Because cryolite will dissolve most potential wall materials, a layer of frozen cryolite must be formed on the walls of the vessel to contain the bath, and this requires the achievement of a delicate heat balance in the cell, over which the recirculatory flows in the bath have an important influence.

There has been, and will continue to be, intensive research for a better understanding of the process, which will assist in the design and optimisation of the process to give improved capacity, operational efficiency, energy saving and environmental impact.

Recently, many pre-baked carbon anodes have incorporated a slot, in order to release bubbles quickly from beneath the anode and hence reduce voltage drop (Tandon and Prasad, 2005; Dias and de Moura, 2005). The implementation of slots demands a comprehensive understanding of their effect on bath flow, as the bath flow significantly affects alumina dissolution and heat balance.

Detailed investigation of bath flow cannot be made using the aluminium reduction cell itself: the ability to take detailed measurements in real cells is limited because of the high temperature, hostile chemical environment (cryolite) and difficulty of access. Furthermore, the ability to trial unusual operating conditions is constrained by the need to maintain control over the cell operation. Physical and numerical modelling provides the opportunity to determine flows, temperature distributions, current density distributions, etc in great detail, and the ability to trial changes to operating conditions and geometrical configurations without risk.

Physical modelling of bubble-driven flow of bath in aluminium cells using water models has been carried out for many years, but mostly using qualitative methods. Advanced Laser Doppler Anemometry (LDA) and Particle Image Velocimetry (PIV) techniques using more powerful lasers and improved software now allow detailed velocity measurements to be taken, even in bubbly regions of the flow.

CFD modelling has also progressed substantially in recent years: greater computing speed, improved software and multiphase algorithms allow prediction of complex flows such as those encountered in aluminium cells, which previously could not have been achieved.

The combination of CFD and physical modelling is much more powerful than either used in isolation because of the

complementary nature of the two methods. Physical modelling has the advantage of being carried out on a real system, but exact similarity to the industrial process can be difficult to achieve and effects such as electro-magnetics, solidification and chemical reactions cannot be taken into account. On the other hand, CFD modelling can account for these complexities and the actual fluid properties, but is based on mathematical equations that need to be validated. CSIRO Minerals (Schwarz, 1994) pioneered the coupled use of CFD and physical modelling to make the best use of the strengths of each technique: CFD models are validated using water modelling and other data, and then provide a dependable basis for carrying out plant design and optimisation. Using this methodology, a wide range of variations in physical design and operational parameters can be tested and refined until a set that gives optimum performance is identified.

This paper presents an application of the coupled use of CFD and physical modelling in the investigation of bath flow of aluminium reduction cells. A time-averaged (steady state) bubble driven flow model has been developed using a full scale air-water model of part of an aluminium reduction cell as a test-bed. The model description and its implementation are detailed in the next section, followed by a comparison of simulated results with experimental data taken under similar conditions using Particle Image Velocimetry (PIV) measurements. Finally, the overall flow in the ACD, the space beneath the anode (referred to as the anode cathode distance, or ACD), has been investigated in terms of streamlines calculated from the CFD simulation and PIV measurement.

MODELLING METHOD

CFD model description

Generally, bubbling flow can be modelled at different time and length scales: at the individual bubble level and at the macro level by local averaging. The former approach tracks the interfaces around each of the bubbles using for example the VOF method, and detailed transient bubbling behaviour can be obtained; however this model requires a very fine mesh that presents a major hurdle for current computing powers. The locally averaged model represents the flow field averaged over time and hence steady state equations are solved. The model also averages over small-scale phase structure (i.e. bubbles) using the so-called two-fluid or Eulerian-Eulerian approach, where gas and liquid are described as interpenetrating continua and equations for conservation of mass and momentum are solved separately for each phase. The model requires less computing power, but the detailed bubbling hydrodynamics can not be obtained. The former model is suitable for fundamental studies, the latter for process simulation, and has been widely used in various multiphase flow systems, e.g. gas stirred baths (Schwarz and Turner, 1988; Lane et al., 2005).

The time averaged two fluid modelling approach has been adopted for this study. The governing equations are the continuity and Navier-Stokes equations, essentially conservation equations for mass and momentum, slightly modified from case to case. For this study, they are given as:

Conservation of mass:

$$\nabla \bullet (\gamma_\alpha \rho_\alpha U_\alpha) = 0 \tag{1}$$

Conservation of momentum:

$$\nabla \bullet (\gamma_\alpha (\rho_\alpha U_\alpha \otimes U_\alpha)) = -\gamma_\alpha \nabla P_\alpha + \nabla \bullet (\gamma_\alpha \mu_\alpha (\nabla U_\alpha + (\nabla U_\alpha)^T)) + S_{M\alpha} + M_\alpha \tag{2}$$

where γ_α is the volume fraction of phase α (either gas or water), ρ_α, U_α are the density and vector velocity for phase α, and P and μ are the pressure and effective viscosity. $S_{M\alpha}$ describes momentum sources due to external body forces, e.g. buoyancy and electromagnetic force (the electromagnetic force is not included in the water flow model). M_α describes the interfacial momentum transfer between phases and can include several types, such as the drag force, lift force, virtual mass, wall lubrication force, inter-phase turbulent dispersion force, etc. The effective viscosity is the sum of molecular (dynamic) viscosity (μ_0) and turbulent viscosity (μ_t).

Phase dependent turbulence models have been used: the dispersed phase zero equation model for gas phase and the k-ε two-equation model for the liquid phase. The turbulence eddy viscosity is calculated as:

$$\mu_{td} = \frac{\rho_d}{\rho_c} \frac{\mu_{tc}}{\sigma} \tag{3}$$

for the gas phase and :

$$\mu_{tc} = c_\mu \rho_c \frac{k_c^2}{\varepsilon_c} \tag{4}$$

for the liquid phase.

The subscript c denotes the continuous liquid phase and d denotes the dispersed gas phase. The parameter σ is a turbulent Prandtl number relating the dispersed phase kinematic eddy viscosity to the continuous phase kinematic eddy viscosity. c_μ is the k-ε turbulent model constant (default value 0.09), and k and ε stand for turbulence kinetic energy and turbulence dissipation rate respectively. As is standard practice, the transport equations for k and ε are assumed to take a form similar to the single-phase transport equations:

$$\nabla \bullet (\gamma_\alpha (\rho_\alpha U_\alpha k_\alpha) - (\mu + \frac{\mu_{t\alpha}}{\sigma_k}) \nabla k_\alpha)) = \gamma_\alpha (P_\alpha - \rho_\alpha \varepsilon_\alpha) + T_{\alpha\beta}^{(k)} \tag{5}$$

$$\nabla \bullet (\gamma_\alpha (\rho_\alpha U_\alpha \varepsilon_\alpha) - (\mu + \frac{\mu_{t\alpha}}{\sigma_\varepsilon}) \nabla \varepsilon_\alpha)) = \gamma_\alpha \frac{\varepsilon_\alpha}{k_\alpha} (C_{\varepsilon 1} P_\alpha - C_{\varepsilon 2} \rho_\alpha \varepsilon_\alpha) + T_{\alpha\beta}^{(\varepsilon)} \tag{6}$$

where $C_{\varepsilon 1}$, $C_{\varepsilon 2}$, σ_K, σ_ε are turbulence model constants, default values being 1.44, 1.92, 1.0 and 1.3 respectively. P_α is the turbulence production due to viscous production. $T_{\alpha\beta}^{(k)}$ and $T_{\alpha\beta}^{(\varepsilon)}$ represent inter-phase transfer for k and ε respectively.

Bubbles rising in the molten bath will also give rise to increased turbulence of the liquid phase, known as bubble-induced turbulence. Bubble-induced turbulence is still an active area of research, as reviewed by Sokolichin et al. (2004). Various models have been proposed in the literature to account for this mechanism, with the two most widely accepted being the Sato and Sekoguchi (1975) model and the turbulence production model. In the Sato and Sekoguchi model, an additional term of the following form is added to the effective viscosity:

$$\mu_{tp} = C_{\mu p} \rho_c (1 - \gamma_c) d_p (U_c - U_d) \tag{7}$$

where $C_{\mu p}$ is the bubble induced turbulent eddy viscosity coefficient.

The second method takes into account the production of turbulence as a source term in the k-ε equations, where various forms have been proposed in the literature. After some trial tests, the first approach was used for this study.

A turbulence dispersion force is proposed in the literature to account for the diffusion of bubbles due to the random influence of turbulent eddies in the liquid. The Favre averaged turbulence dispersion force model, an option in the CFX10 Solver, has been used in this study. The form is given as:

$$M_c^{TD} = -M_d^{TD} = -C_{TD}C_{cd}\frac{\upsilon_{tc}}{\sigma_{tc}}\left(\frac{\nabla\gamma_d}{\gamma_d} - \frac{\nabla\gamma_c}{\gamma_c}\right) \tag{8}$$

Unfortunately, universally applicable values of C_{TD} for this model have not been found in studies reported in the literature (Moraga et al., 2003). In this project, physical measurements are used to help determine an appropriate value and this is discussed later.

PIV measurement

Particle Image Velocimetry (PIV) is a whole-flow-field technique providing instantaneous velocity vector measurements in a cross-section of a flow. Two velocity components are measured by taking two images within a short time interval and determining the displacement of the tracer particles travelled within the time. The use of modern CCD cameras and dedicated computing hardware result in real-time velocity maps. Detailed description of the principles of the PIV system can be found in Raffel et al. (1998).

CSIRO Minerals has used an ILA 2D PIV system to study various single phase or multiphase systems, both independently (Cooksey and Yang, 2006) and/or in combination with CFD modelling (Bujalski et al., 2006).

Model parameters

The CFD modelling setup was based on a water model, which has been constructed to study the effect of anode slots and inter-anode gap on liquid flow in part of a cell. A diagram of the physical model (constructed of Perspex) is shown in Figure 1. The detailed configuration can be found in a previous publication (Cooksey and Yang, 2006). A few key parameters are described here for convenience of discussion.

The anode dimensions (1300 mm x 650 mm x 600 mm) were selected to be the same as those typical of a modern pre-bake smelter (not a specific anode design), which is helpful because it is notoriously difficult to maintain dynamic similarity in such strongly multi-phase systems when the scale is much smaller. Other parameters were set as follows:

ACD (anode-cathode distance):	40	mm
Anode slope:	0°	
Tap-end channel:	160	mm
Duct-end channel:	40	mm
Side channel:	240	mm
Centre channel:	120	mm
Liquid depth, H:	200	mm
Gas flow rate for each anode:	120	L/min

In addition to the four vertical planes (Locations (A) to (D)), measurement has also been made in a horizontal plane half-way between the bottom of the anodes and the base of the model, i.e., the mid-point of the ACD.

To obtain a numerical solution, the geometry was first meshed into discrete elements, using the CFX meshbuilder platform, followed by setting the following boundary conditions:

- a gas inlet to the computational domain on the bottom surface of the anode representing gas generation by reduction;
- a gas outlet on the top surface of the liquid pool at which gas leaves the bath at the rate it arrives from below (i.e. a so-called "degassing condition");
- the other solid boundaries were set as walls (no slip for water and free slip for air).

On the basis of observation of the water model, bubble size was taken to be 0.01 m in diameter, and uniform. The bubble induced turbulent eddy viscosity coefficient $C_{\mu p}$ (see Eq. (7)) and the turbulence dispersion force coefficient C_{TD} (see Eq. (8)) were set to 20 and 0.1 respectively. On the basis that turbulent motion of bubbles under the anode is strongly suppressed by the anode, C_{TD} was set to 0 in this region and no bubble-induced turbulence term was added in this area. These coefficients are poorly known, so effort has been required to optimise the values to achieve agreement with experimental measurements. Due to the lack of information concerning drag forces for bubbles moving under a horizontal surface, as stated in previous publication (Solheim et al., 1989), the same drag force correlation has been applied to the whole cell. Momentum exchange through drag force is calculated according to Ishii and Zuber (1979) correlations, which are readily available in the CFX solver.

Solution of these equations was carried out using a commercial CFD code (ANSYS-CFX10), facilitated by some user-defined subroutines.
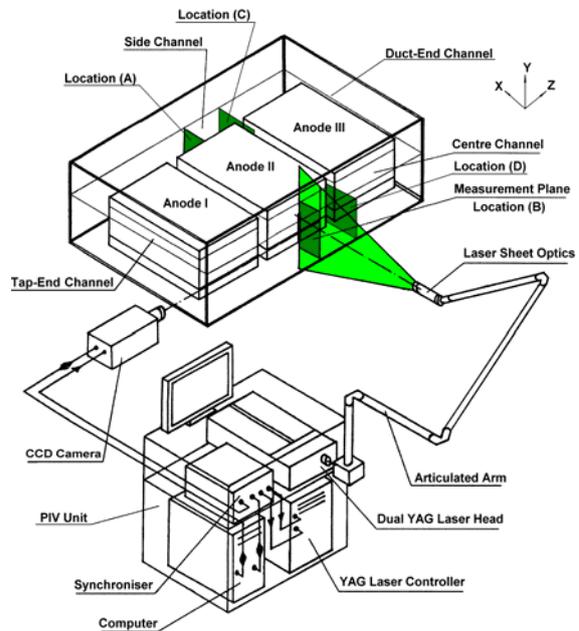
Figure 1: Three-anode physical model, showing arrangement of PIV measurement for vertical planes.

RESULTS AND DISCUSSION

As the first stage of CFD model development, this paper focuses on validation of the CFD model through

comparison between CFD and PIV measurement over four vertical planes as shown in Figure 1, and one horizontal plane at the mid-point of the ACD.

We first discuss measurements taken in the side channel, at the mid-point of Anode II (Figure 2, location (A) in Figure 1). Bubbles released from the anode bottom change direction and rise upward at the anode edge due to the buoyancy force. Consequently, water is pumped upward, and flows almost vertically. The water flow changes direction horizontally toward the outer wall at the liquid surface, followed by a vertically downward flow close to the outer wall, completing the recirculation by joining the upward flow. A similar flow pattern can be observed from both CFD simulation and PIV measurement, particularly in the position of the centre of the recirculation zone that appears close to the left top corner. A reverse flow towards the ACD has been observed from CFD simulation, but is not clear from PIV measurement, as there is no data from PIV measurement. PIV measurement in the horizontal plane at the mid-point of the ACD (discussed later) confirms this type of reverse flow.

Figure 3 compares the water velocity field over a vertical plane at the mid-point of Anode II in the centre channel. (location (B) in Figure 1). As in the side channel, bubbles released from the anode bottom pump water up almost vertically near the anode; water flows towards the ACD from the bottom of the centre channel; and a recirculation forms in the centre channel. The centre channel width is about half the side channel width. This affects the details of flow, e.g. the position of the centre of swirl. In general the flow patterns from the CFD simulation (Figure 3 (a)) are very similar to the PIV measurement (Figure 3 (b)).

Figure 4 and Figure 5 show the water flow in vertical planes at the mid-point of the inter-anode gap (locations

(C) and (D) respectively in Figure 1). Bubbles released into the inter-anode gap pump water towards both the side channel (Figure 4) and the centre channel (Figure 5). Both CFD simulation and PIV measurement show a backflow from the side channel towards the ACD (Figure 4). At the bottom of the centre channel, CFD predicts a water flow from the ACD towards the centre channel, while PIV measurement shows almost no flow (Figure 5).

Figure 6 compares the water flow in a horizontal plane at the mid-point of ACD. Streamlines have been plotted to identify the overall flow that is more complex than might be expected. Despite this complexity, there is good overall similarity between the predicted and measured flow patterns. Obviously, a point-wise match between simulation and measurement is not possible, as there are many sources of uncertainty in both the physical and numerical models. For example, small irregularities in the surface of the model anode were found to significantly affect the bubble distribution in the physical model. Similarly, the fixed bubble size used in the CFD model cannot reflect all of the real physics, e.g. coalescence and breakup. However, in terms of overall flow, the CFD simulation predicts a similar flow pattern to the PIV measurement. For example, water flows towards the ACD from the wider end channel (tap-end) and flows out from the ACD at the narrower end channel (duct-end); the low velocity is much stronger in the side and centre channels than beneath the anode.

Overall, agreement between measurements and model results is good, given the complexity of the flow and the uncertainties in velocity measurement in the bubble region.
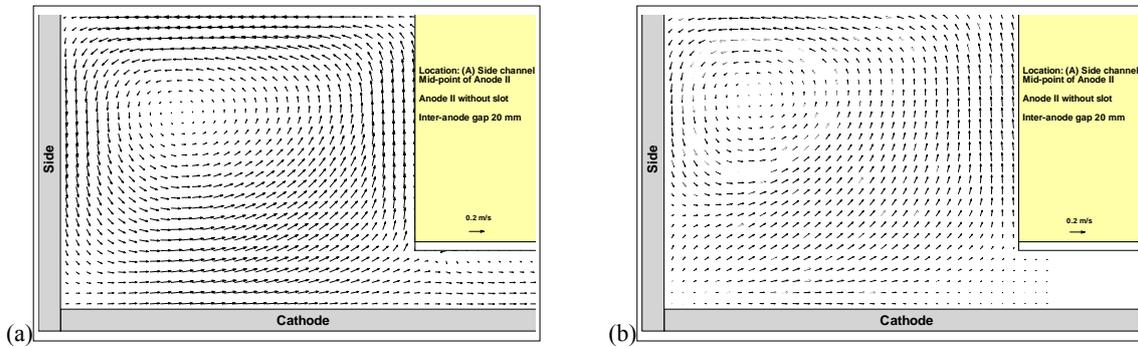
Figure 2: Water velocity distribution at location (A) in figure 1: (a) CFD simulation; (b) PIV measurement.
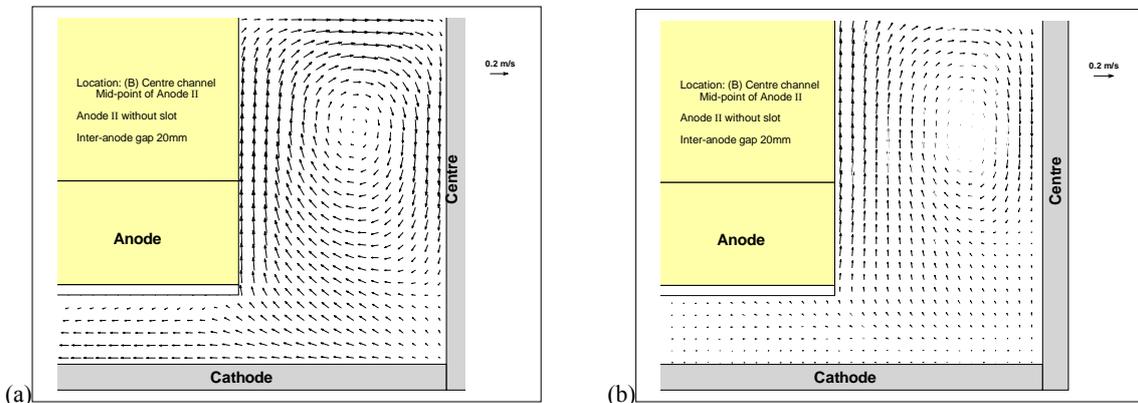
Figure 3: Water velocity distribution at location (B) in figure 1: (a) CFD simulation; (b) PIV measurement.
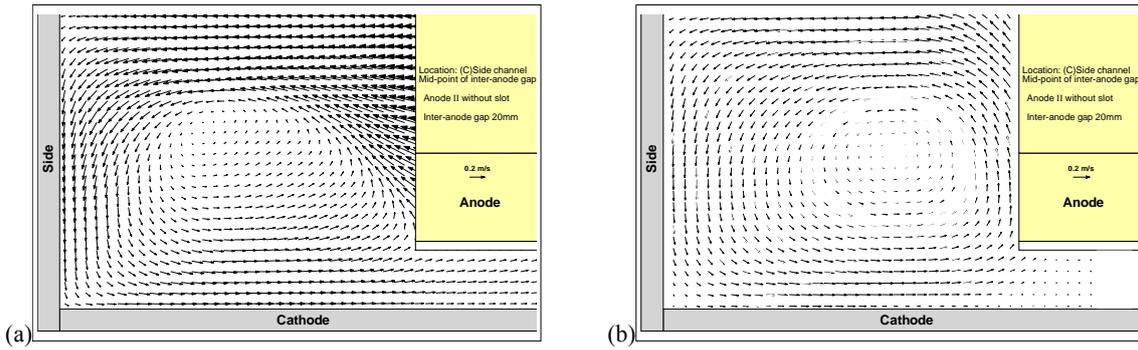
Figure 4: Water velocity distribution at location (C) in figure 1: (a) CFD simulation; (b) PIV measurement.
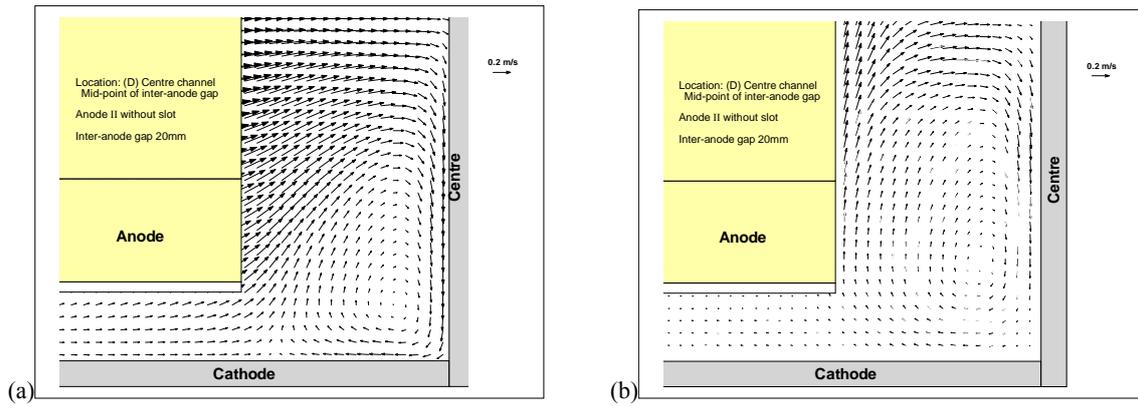
Figure 5: Water velocity distribution at location (D) in figure 1: (a) CFD simulation; (b) PIV measurement.
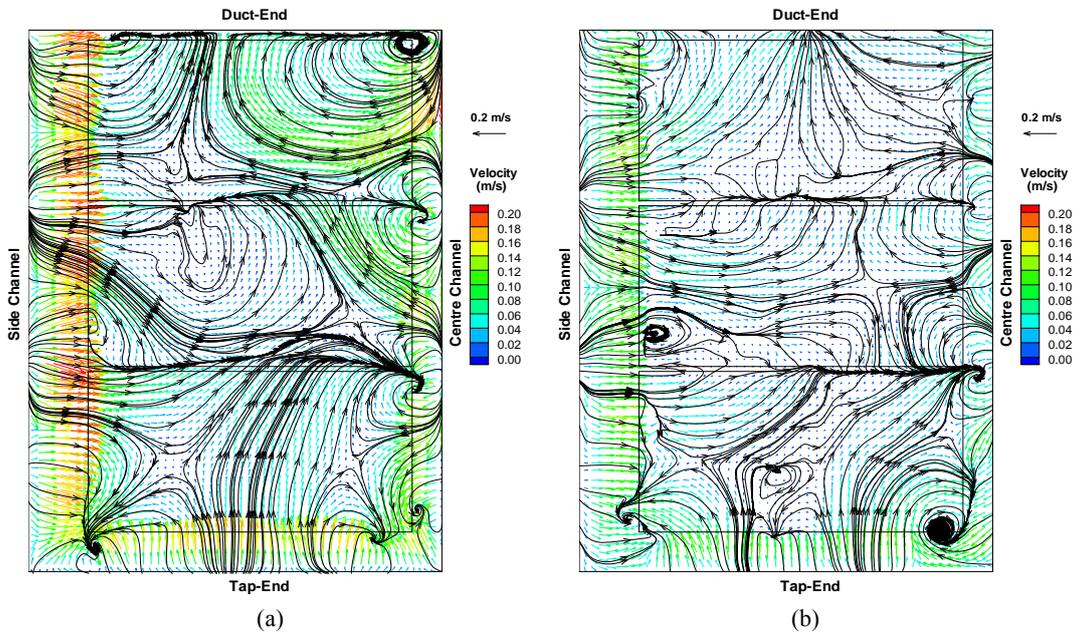
Figure 6: Water velocity distribution over a horizontal plane in the middle of the ACD: (a) CFD simulation; (b) PIV measurement.

CONCLUSION

A CFD model of the bubble driven hydrodynamics in aluminium reduction cells has been developed and compared with PIV measurements taken under similar conditions. Good agreement has been obtained between the CFD model and the PIV measurements, demonstrating the validity of using the CFD model to study the effect of various design parameters (e.g. inter-anode gap, presence of a slot) on bath flow in an industrial cell.

The overall flow in the ACD has been investigated in terms of streamlines. It was found that the water flow is very complex, involving local and global recirculation. Local mixing has been identified both in side and centre channels as visualized by recirculations and in the ACD depicted by streamlines, while global mixing can be achieved, as evidenced by the flow in the ACD from wider end channel (tap-end) towards the narrower end channel (duct-end).

ACKNOWLEDGEMENTS

REFERENCES

ANSYS CFX 10 User manual, ANSYS Inc.

BUJALSKI JM, YANG W, NIKOLOV J, SOLNORDAL CB, and SCHWARZ MP, (2006), "Measurement and CFD simulation of single-phase flow in solvent extraction pulsed column", Chemical Engineering Science, **61**, 2930-2938.

COOKSEY, M.A. and YANG, W., (2006), "PIV measurements on physical models of aluminium reduction cells", Light Metals, 359-365.

DIAS, H.P. and DE MOURA, R.R., (2005), "The use of transversal slot anodes at Albras smelter", Light Metals, 341-344.

ISHII, M. and ZUBER, N., (1979), "Drag coefficient and relative velocity in bubbly, droplet or particulate flows", AIChE J., **25**, 843-855.

LANE, G. L., SCHWARZ, M. P., and EVANS, G. M., (2005). "Numerical modelling of gas-liquid flow in stirred tanks", Chemical Engineering Science, **60**, 2203-2214.

MORAGA, J.F., LARRELEGUY, A.E., DREW, D.A. and LAHEY, R.T., (2003), "Assessment of turbulent dispersion models for bubbly flows in the low stokes number limit", Int. J. Multiphase Flow, **29**, 655-673.

RAFFEL, M., WILLERT, C.E. and KOMPENHANS, J., (1998), "Particle Image Velocimetry: a practical guide", Springer-Verlag Berlin Heidelberg, New York.

SATO, Y. and SEKOGUCHI, K., (1975), "Liquid velocity distribution in two-phase bybbly flow", Int. J. Multiphase Flow, **2**, 79.

SCHWARZ, M.P., (1994), "The role of computational fluid dynamics in process modelling", 6th AusIMM Extractive Metallurgy Conf., pp. 31-36.

SCHWARZ, M.P. and TURNER, W.J., (1988), "Applicability of the standard k-ε turbulence model to gas-stirred baths", Appl. Math. Modelling, **12,** 273-279.

SOKOLICHIN, A., EIGENBERGER, G. and LAPIN, A., (2004), "Simulation of buoyancy driven bubbly flow: established simplifications and open questions", 50, 24-44.

SOLHEIM, A., JOHANSEN, S.T., ROLSETH, S. and THONSTAD, J., (1989), "Gas induced bath circulation in aluminium reduction cells", Journal of Applied Electrochemistry, **19**, 703-712.

TANDON, S.C. and PRASAD, R.N., (2005), "Energy savings in Hindalco's Aluminium smelter", Light Metals, 303-309.